



Programmable skyrmion-based logic gates in a single nanotrack

Laichuan Shen ¹, Yan Zhou,² and Ka Shen ^{1,*}

¹The Center for Advanced Quantum Studies and Department of Physics, Beijing Normal University, Beijing 100875, China

²School of Science and Engineering, The Chinese University of Hong Kong, Shenzhen, Guangdong 518172, China



(Received 29 November 2022; revised 6 February 2023; accepted 13 February 2023; published 27 February 2023)

Programmable logic devices with multiple functions are key ingredients in information technology. Here we propose a multifunction logic device based on the current-driven skyrmion motion in a single nanotrack, where the spatially modulated Dzyaloshinskii-Moriya interaction introduces a potential barrier to the skyrmion. Three stable stages of the skyrmion location under a driving current of different magnitudes are demonstrated at room temperature through micromagnetic simulations, according to which we implement all necessary logic gates for computing applications. Our proposal provides a feasible scheme to design skyrmion-based programmable logic devices.

DOI: [10.1103/PhysRevB.107.054437](https://doi.org/10.1103/PhysRevB.107.054437)

I. INTRODUCTION

Logic gates are basic units of electronic computing devices. In recent years, magnetic logic gates potentially with low power consumption, nonvolatility, and programmable logic operations, have received increasing research interest [1–3]. So far, various types of conceptual magnetic logic devices have been proposed, based on magnetization switching [4–7], magnetic domain wall motion [3,8], spin wave transmission [9–11], or magnetic skyrmion dynamics [12–26]. Among them, magnetic skyrmions, stable particlelike topological spin textures, are believed to be promising candidates for the next generation of realistic computing devices [27–36]. While most proposals of skyrmion-based logic gates only allow a specific logic operation in one device [12–15], programmable designs with multiple logic functions [16,22,23] could not only provide a much higher flexibility in applications but also open opportunities to reduce the size and cost of integrated circuits.

In practice, various skyrmion-based logic operations, including AND, OR, NOT, NAND, NOR, XOR, and XNOR, were theoretically demonstrated to be achievable in a single structure by selectively activating the inputs/outputs [16,22] or electrically manipulating material parameters, such as the magnetic anisotropy and Dzyaloshinskii-Moriya interaction (DMI), along the skyrmion nanotrack [16,23]. The experimental realization of such devices, however, requires the fabrication of a set of control gates or circuits within a nanoscale working structure [16,18,21,23], which might cause additional technical challenges and manufacturing cost. The effectiveness and the efficiency of the modification in the material parameters by nanoscale gates spatially close with each other are also questionable. An easily accessible design for reconfigurable skyrmion-based multifunction devices is therefore desirable.

In the present work, we demonstrated through micromagnetic simulation that a single nanotrack containing a potential barrier in the skyrmion pathway, as schematically illustrated in Fig. 1(a), is sufficient to perform various logic operations by current-induced motion of the skyrmion locally created on one side of the nanotrack. As the barrier defines spatially two local minima of the skyrmion potential energy, under a driving current pulse above a critical value, the initialized skyrmion could pass through the barrier and resides on the other side unless the driving current is too large to destroy the skyrmion at the boundary. The existence of the two critical currents for skyrmion climbing over the barrier and annihilating at the boundary, as we will explicitly show below, allows multiple logic functions, such as, namely AND, OR, XOR, NAND, NOR, XNOR, and NOT, to be performed based on proper control of the driving current via input signals. In contrast to previous proposals, no manipulation on the geometry or material parameters of the magnetic working layer is needed during the switching among the logic functions in our device.

II. DEVICE STRUCTURE AND SKYRMION DYNAMICS

As explicitly depicted in Fig. 1(a), our skyrmion nanotrack is based on a heterostructure consisting of a ferromagnetic working layer and a nonmagnetic heavy metal. The latter, labeled as HM1, is employed to introduce, on one hand, an interfacial DMI (parameterized by D_1) to the ferromagnetic layer to stabilize the skyrmion therein and, on the other hand, a spin-orbit torque for current-induced skyrmion motion [31]. As the potential barrier may be established by different approaches, we here consider a local change in the DMI parameter, which is achievable experimentally by, for instance, locally modifying the properties of the heavy metal [38,39], utilizing local ion irradiation on the magnetic layer [40], applying an electric field normal to the interface [41], or modulating the interface between the magnetic layer and heavy metal [42]. Specifically, a heavy metal strip (labeled as HM2) grown on top of the ferromagnetic

*kashen@bnu.edu.cn

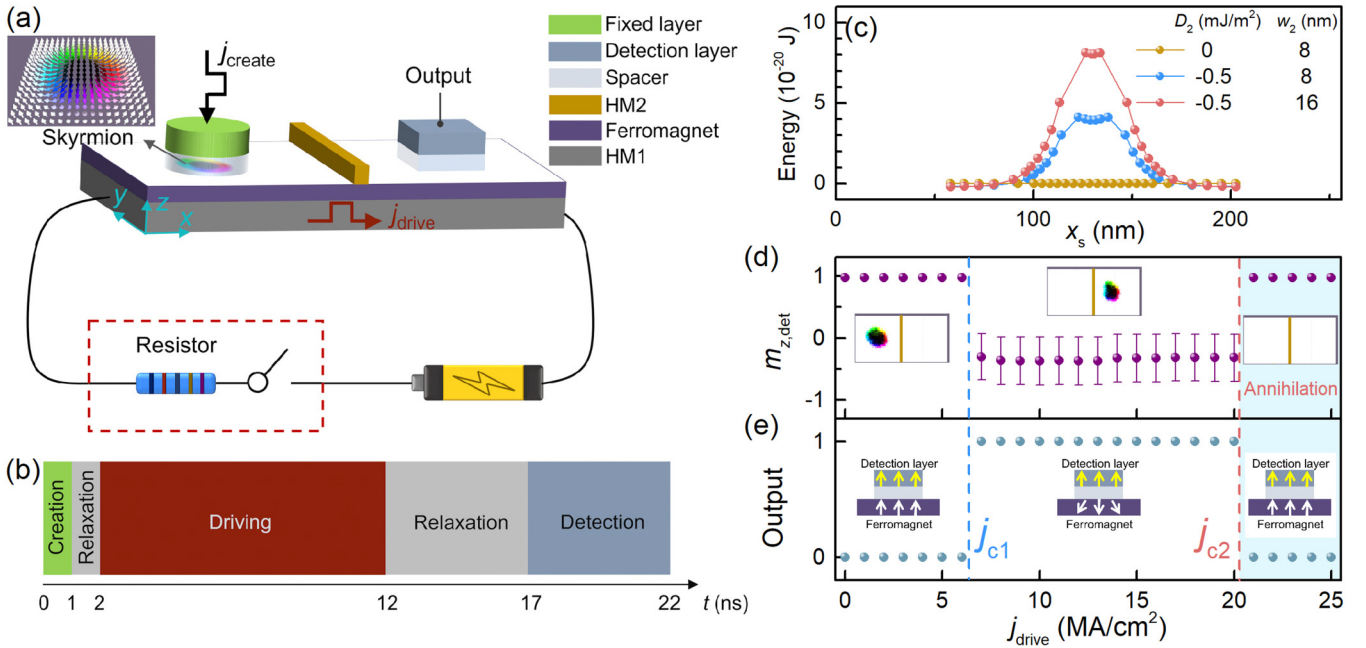


FIG. 1. (a) Schematic of the skyrmion nanotrack. The heavy metal (HM1) and ferromagnet constitute a nanotrack with a locally modulated DMI due to the heavy metal strip (HM2). The spacer and perpendicularly magnetized fixed layer on the left side of the nanotrack are used to create the skyrmion via the current-induced spin transfer torque. The detection layer (a reference magnetic layer), spacer, and ferromagnet together form a spin valve structure that can characterize the orientation of the ferromagnetic magnetization by means of the magnetoresistance effect. The skyrmion dynamics is triggered by an in-plane driving current in HM1. (b) The entire operation sequence in our micromagnetic simulation. (c) The DMI-induced potential energy as a function of the skyrmion position x_s , with different DMI strengths (D_2) and the widths (w_2) of the HM2 strip. (d) Recorded magnetization $m_{z,det}$ of the working layer in the 40×40 nm² detection area and (e) the logic output as functions of the driving current j_{drive} . In the simulation for (d) and (e), we use $\alpha = 0.5$ [37] and $T = 300$ K. w_2 and D_2 are adopted to be 8 nm and -0.5 mJ/m², respectively. Error bars in panel (d) represent the standard derivation, and the insets show the snapshots of representative magnetization configurations. The insets in panel (e) are the magnetization configurations of the ferromagnet and detection layer. j_{c1} and j_{c2} are the critical current densities for the transitions between different spin configurations.

working layer is adopted to partially compensate the DMI induced by HM1 [38]. The resulting energy barrier can be clearly recognized from Fig. 1(c), where the skyrmion potential energy with typical material parameters is plotted as a function of the skyrmion location. The technical details for this calculation are presented in Appendixes A and B. The shaped magnetic fixed layer in Fig. 1(a) is used to create the skyrmion via the current-induced spin transfer torque [43]. The detection layer uniformly magnetized along z direction reads out the final magnetization in the detection area of the working layer through the magnetoresistance effect [44].

The dynamics of the skyrmion in the working layer, including its creation and current-induced motion, with realistic material parameters are carried out from micromagnetic simulation (see Appendix A for the details). Figure 1(b) illustrates the operation sequence. Starting from a ferromagnetic ground state of the working layer, a skyrmion is created on the left side of the nanotrack by injecting a current pulse (j_{create}) through the fixed layer [36]. After a waiting time (~ 1 ns) for relaxing the skyrmion texture, an in-plane current (j_{drive}) with a duration of 10 ns is applied in HM1 to drive the skyrmion motion. The output is extracted after another waiting time (5 ns).

The readout signal, i.e., the average out-of-plane magnetization in the detection region ($m_{z,det}$), is plotted in Fig. 1(d)

as a function of the driving current j_{drive} . Below the critical value $j_{c1} \simeq 6.3$ MA/cm², the driving current is too small to overcome the potential barrier so that the skyrmion remains on the left side (see the left inset). Above j_{c1} , the skyrmion passes through the barrier to the right side of the nanotrack. If the driving current is too large, however, the skyrmion will be annihilated at the nanotrack boundary, which defines the upper critical value $j_{c2} \sim 20.2$ MA/cm² and hence a finite window $j_{c1} \leq j_{drive} < j_{c2}$ for the final configuration with the skyrmion locating on the right side (see the middle inset). Within this window, the skyrmion finally resides in the detection area, leading to its magnetization being nearly antiparallel to that of the detector (assumed to be along the z direction), which we define as the logic output “1” [see Fig. 1(e)]. For a driving current outside the above window, i.e., $j_{drive} < j_{c1}$ or $j_{drive} \geq j_{c2}$, there is no skyrmion in the detection area and thus $m_{z,det} \simeq 1$, meaning that the magnetization remains parallel to that of the detection layer, giving an output “0”. Such a step-shaped dependence of the output supplies a good platform for designing logic gates. For example, by reversing the magnetization direction of the detection layer to the $-z$ direction and choosing a driving current within the window, the final skyrmion location after the input “1” (“0”), naturally defined as the condition with (without) an input current, gives an output “0” (“1”), realizing the one-input NOT gate.

TABLE I. Truth table of the basic logic gates XOR, AND, OR, XNOR, NAND, and NOR. I_1 and I_2 represent the two logic inputs.

(I_1, I_2)	XOR	AND	OR	XNOR	NAND	NOR
(0, 0)	0	0	0	1	1	1
(0, 1)/(1, 0)	1	0	1	0	1	0
(1, 1)	0	1	1	1	0	0

III. TWO-INPUT LOGIC OPERATIONS

In this section we show how the device works as two-inputs logic gates following the truth table in Table I. As the logic inputs “1” and “0” are defined as the presence and absence of a certain driving current from one specific lead, the main task is actually to find out a proper magnitude of the two input currents (j_1, j_2) as the driving source of skyrmion motion for each logic function. For the AND gate, the input currents $(j_1, j_2) = (0, 0)/(0, j_{in})/(j_{in}, 0)$ yield the logic output “0”, which requires $j_{in} < j_{c1}$ according to Fig. 1(e). On the other hand, the logic output should be “1” for the input $(j_1, j_2) = (j_{in}, j_{in})$, meaning that the total current $(j_1 + j_2 = 2j_{in})$ must fall into the window between the two critical values, i.e., $j_{c1} \leq 2j_{in} < j_{c2}$. From these two conditions, we obtain the range of the proper j_{in} for the AND gate, described as $0.5j_{c1} \leq j_{in}^{AND} < \min\{j_{c1}, 0.5j_{c2}\}$. For the OR gate, the output is “0” for $(j_1, j_2) = (0, 0)$ and “1” for $(0, j_{in})/(j_{in}, 0)/(j_{in}, j_{in})$, requiring $j_{c1} \leq j_{in} < j_{c2}$ and $j_{c1} \leq 2j_{in} < j_{c2}$, from which we find $j_{c1} \leq j_{in}^{OR} < 0.5j_{c2}$. This expression implies that the two critical currents should satisfy the condition $j_{c1} < 0.5j_{c2}$ for the implementation of the OR gate. For the XOR gate, the range of the proper j_{in} is $\max\{j_{c1}, 0.5j_{c2}\} \leq j_{in}^{XOR} < j_{c2}$ derived from $j_{c1} \leq j_{in} < j_{c2}$ and $2j_{in} \geq j_{c2}$. The current ranges for these three operations are summarized in Fig. 2(a).

To establish the relationship between the logic inputs (“0” and “1”) and the magnitude of driving currents, we replace the resistor part for current control [the red box in Fig. 1(a)] by a parallel subcircuit with a pair of identical resistors and two switches [see Figs. 2(b)–2(d)]. The “on” and “off” of each switch stand for logic inputs “1” and “0”, respectively. In such

a parallel circuit, obviously, the current increases with the number of on-state switches. Since different driving current strengths are required for the three logic gates, we consider three pairs of resistors with different resistances connected together in a single parallel circuit to regulate the current. In the case of Fig. 1(e), $0.5j_{c2}$ (~ 10.1 MA/cm²) is greater than j_{c1} (~ 6.3 MA/cm²), so that the AND, OR, and XOR gates can be realized when j_{in} is in the range $[3.15, 6.3)$, $[6.3, 10.1)$, and $[10.1, 20.2)$ MA/cm², respectively, according to Fig. 2(a). We take $j_{in} = 5, 8,$ and 12 MA/cm² as examples in our micromagnetic simulation to demonstrate the realization of the AND [Fig. 2(b)], OR [Fig. 2(c)], and XOR [Fig. 2(d)] gates, respectively.

As indicated in Table I, the AND, OR, and XOR gates will be transformed to the NAND, NOR, and XNOR gates, respectively, if the corresponding logic outputs are reversed. This can be achieved directly by switching the magnetization of the detection layer [16,23] or by flipping uniformly the ferromagnetic magnetization in the initialization process. If one chooses to flip the magnetization of the detector, then all the logic functions can be performed from the same initial magnetization configuration of the working layer. The one-input NOT gate thus is feasible by taking one of the switches in the circuit of the XNOR or NOR gate as the input control, which provides a proper j_{in} between j_{c1} and j_{c2} . The operations of a specific logic function include (i) injecting a current into the fixed layer to prepare the initial skyrmion state, (ii) manipulating the magnetization of the detector and operating the switches in the parallel circuit to regulate the driving currents matching the requested logic function, and (iii) reading out the magnetoresistance signal from the detector.

Note that the skyrmion is annihilated by the boundary at the right end after applying the inputs (1, 1) in the XOR gate. As shown in Appendix C, by introducing a second potential barrier to trap the skyrmion leaving the detection area, a conservative design (with skyrmion number conserved in the whole device) can be achieved.

IV. PARAMETER CONTROL

According to Fig. 2(a) and the discussion above, we already see that the values of the two critical current densities j_{c1} and j_{c2} are crucial for realizing a complete set of logic operations. Therefore, in this section we analyze their dependences on material parameters.

The influences of the damping constant α are summarized in Fig. 3(a) with three scenarios (with/without material inhomogeneity at different temperatures). As one can see, j_{c1} and j_{c2} in each case both decrease with the decrease of α , because of the enhanced driving efficiency at a smaller damping constant [15]. For the homogeneous case at zero temperature, as shown by the yellow bullets, j_{c1} is close to j_{c2} , resulting in a rather small current range for AND and XOR gates, according to Fig. 2(a). More seriously, the OR gate cannot be achieved because $0.5j_{c2} \leq j_{c1}$. These problems can be solved by increasing the temperature up to room temperature, in which j_{c1} is dramatically suppressed while j_{c2} does not change too much, making $0.5j_{c2} > j_{c1}$. The critical currents with $\alpha = 0.5$ have already shown in Fig. 1(d), and the logic operations in Fig. 2 include the OR function. The decrease of j_{c1} at higher

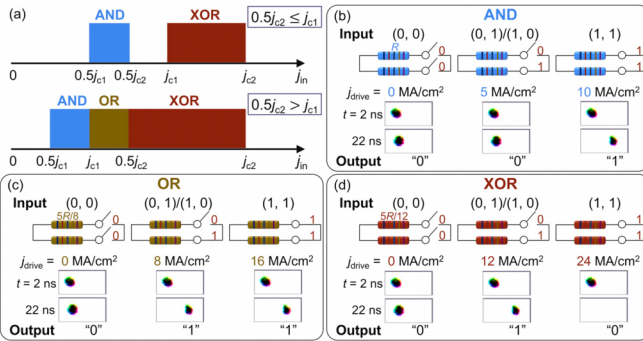


FIG. 2. (a) The ranges of the proper j_{in} for constructing different logic gates with two situations $0.5j_{c2} \leq j_{c1}$ and $0.5j_{c2} > j_{c1}$. Demonstration of the logic operations (b) AND, (c) OR, and (d) XOR at 300 K with $w_2 = 8$ nm and $D_2 = -0.5$ mJ/m². Each resistor in (b)–(d) is taken to be $R, 5R/8,$ and $5R/12,$ respectively, with R being the value given a driving current $j_{in} = 5$ MA/cm².

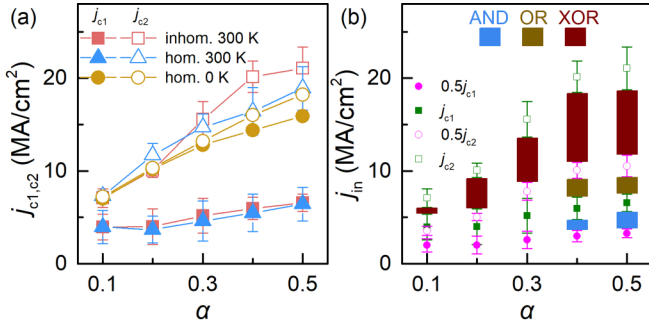


FIG. 3. (a) The critical current densities j_{c1} and j_{c2} as functions of the damping constant α , in three situations (homogeneous ferromagnet at zero temperature and homogeneous/inhomogeneous ferromagnet at 300 K) with $w_2 = 8$ nm and $D_2 = -0.5$ mJ/m². The material inhomogeneity is considered via local modification of the anisotropy constant, as explained in the text. (b) The proper current ranges for AND, OR, and XOR gates with different values of the damping constant in an inhomogeneous working layer at 300 K. The error bars for 300 K represent the standard derivation of the results from five individual calculations with different random number sequences.

temperature reflects the suppression of the effective potential barrier by thermal effects via the modification skyrmion size and thermal fluctuation, of which a detailed analysis can be found in Appendix D. In contrast, j_{c2} is mainly associated with the condition of the nanotrack boundary and therefore is only weakly affected by the thermal fluctuation. Moreover, from the calculation with the randomly modified local anisotropy constant within 15% [45] [see the solid and open squares in Fig. 3(a)], both j_{c1} and j_{c2} at 300 K are found to be robust against the material inhomogeneity.

With the knowledge of j_{c1} and j_{c2} , we sketch out the proper working condition for different damping constants in Fig. 3(b) at 300 K. Note also that, besides the reduction of j_{c1} , the finite temperature also causes thermal fluctuation in both critical currents, as shown by the error bars in Fig. 3(a). To ensure the good performance of the logic operations, such thermally induced uncertainty has been taken into account in determining the ranges of the working currents, as indicated by the colored bars in Fig. 3(b), which suggests that the ferromagnet with a large damping is favorable.

For a further manipulation of the working condition at a given temperature, one may consider tuning the potential barrier by directly modifying the parameters in the barrier region. The estimation in Appendix B gives an approximate expression for the height of the potential barrier as

$$V_{\text{DMI}} \sim -2\pi t_z D_2 w_2, \quad (1)$$

which suggests that the potential barrier and hence the critical current (j_{c1}) to overcome this barrier will decrease with decreasing the width of the HM2 strip (w_2) or the magnitude of its resulting DMI (D_2). The current ranges for logic operations with different values of w_2 and D_2 are summarized in Fig. 4. For a given DMI parameter $D_2 = -0.5$ mJ/m² in Fig. 4(a), a smaller w_2 indeed broadens the current window for the OR gate thanks to the reduction of j_{c1} (j_{c2} mainly determined by the edge properties is insensitive to w_2). However, when the strip width reduces to below 4 nm, j_{c1} becomes too small

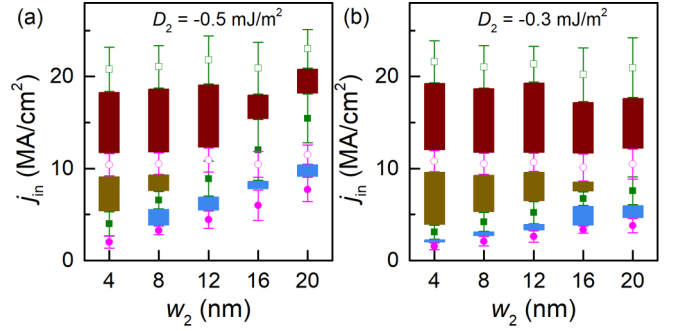


FIG. 4. The proper current ranges for logic operations with different values of strip width w_2 and modifications of the DMI strengths D_2 at 300 K. The meanings of the symbols are the same as those in Fig. 3(b). In the calculation, we consider an inhomogeneous ferromagnet with $\alpha = 0.5$.

to perform the AND operation. For a larger w_2 , j_{c1} goes up quickly, closing the current window for the OR operation. As a result, only a strip around $w_2 = 8$ nm is suitable for realizing AND, OR, and XOR gates in one device. Fortunately, as shown in Fig. 4(b), j_{c1} with a smaller DMI strength becomes less sensitive to the strip width, providing more choices of strip width for complete logic operations.

In addition, the dependence of j_{c2} on the edge properties implies the possibility to further manipulate the working windows by modifying the boundary of the nanotrack. This can be done by, for example, introducing a notch [46,47] and changing the magnetic anisotropy constant [48] or the thickness of the ferromagnetic layer around the material edge [49]. For the conservative design presented in Appendix C, the parameter control of the second metallic bar, the same as we shown in Fig. 4 for the first bar, may also work.

V. DISCUSSION ON PERFORMANCE EVALUATION

According to Ref. [24], the energy consumption during logic operation can be estimated from $E_{\text{op}} = (j_{\text{drive}} S)^2 R_{\text{tot}} \tau_d$, with S being the y - z cross-sectional area of the HM1, R_{tot} the resistance, and τ_d the current duration. R_{tot} mainly consists of two parts, namely, the external resistor and that of HM1. In order to effectively regulate the current, the former (about 1 k Ω) is considered to be much larger than the latter ($R_{\text{HM1}} = \rho L/S \approx 84.8 \Omega$ by substituting the typical resistivity $\rho = 1.06 \times 10^{-7} \Omega\text{m}$ [17], the area $S = 128 \times 2.5$ nm², and the length $L = 256$ nm of the HM1). Taking $j_{\text{drive}} \sim 10$ MA/cm² and $\tau_d = 10$ ns, we have $E_{\text{op}} \sim 10$ fJ. The energy expense for the initialization (skyrmion creation) and detection is mainly determined by Joule heating, estimated to be several femtojoules, according to Ref. [17]. With these considerations, we suppose that the energy consumption of our proposal is comparable to that of other skyrmion-based logic devices [21,24]. The operation time, 22 ns, illustrated in Fig. 1(b), is also at the same level as other skyrmion-based logic proposals [18,21,24] and spin-wave-based logic devices [10].

Our results are carried out with the thermal effects included in micromagnetic simulations, indicating the robustness of our logic operation at finite temperature. Moreover, as shown in Fig. 5, the skyrmion after the operation can retain at its

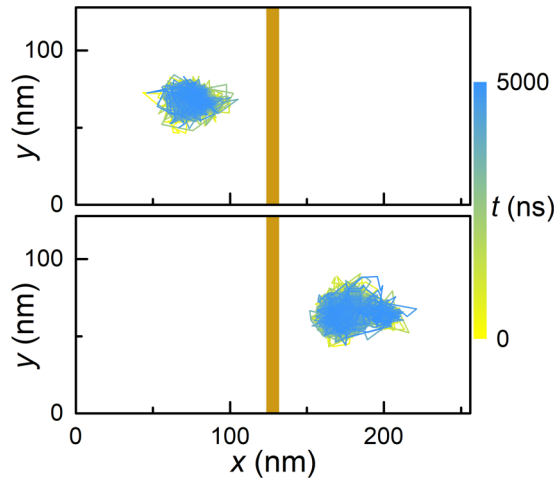


FIG. 5. The trajectories of the skyrmion under thermal effects at 300 K in the absence of driving current. The top and bottom panels show the situations with an initial skyrmion at the left and right sides of the nanotrack, respectively. In this calculation, we use $D_2 = -0.5$ mJ/m² and $w_2 = 8$ nm.

correct location even after 5000 ns (our longest simulation time), reflecting its nonvolatility.

VI. CONCLUSION

In conclusion, we investigate the current-induced skyrmion dynamics in a nanotrack with an energy barrier induced by a local modification in Dzyaloshinskii-Moriya interaction strength. Based on the steplike response of the skyrmion locations on the strength of driving currents, we demonstrate various logic functions, including AND, OR, XOR, NAND, NOR, XNOR, and NOT, and provide the working conditions for each logic operation in a single nanotrack. As the local modification in Dzyaloshinskii-Moriya interaction is considered in this work, our proposal also works for the potential barrier generated by other sources of material inhomogeneities [49–51].

ACKNOWLEDGMENTS

This work is supported by the National Natural Science Foundation of China (Grant No. 11974047) and the Fundamental Research Funds for the Central Universities. Y.Z. acknowledges support from the Guangdong Basic and Applied Basic Research Foundation (Grant No. 2021B1515120047), Guangdong Special Support Project (Grant No. 2019BT02X030), Shenzhen Fundamental Research Fund (Grant No. JCYJ20210324120213037), Shenzhen Peacock Group Plan (Grant No. KQTD20180413181702403), Pearl River Recruitment Program of Talents (Grant No. 2017GC010293), and the National Natural Science Foundation of China (Grants No. 11974298 and No. 61961136006).

APPENDIX A: DETAILS FOR MICROMAGNETIC SIMULATIONS

In this work, the open-source software MUMAX3 [52] is adopted to perform micromagnetic simulation, in which the dampinglike spin torque and the thermal fluctuation are in-

cluded into the Landau-Lifshitz-Gilbert (LLG) equation of reduced magnetization (\mathbf{m}) as [31,53,54]

$$\dot{\mathbf{m}} = -\gamma \mathbf{m} \times (\mathbf{H}_{\text{eff}} + \mathbf{H}_{\text{th}}) + \alpha \mathbf{m} \times \dot{\mathbf{m}} + \gamma H_j (\mathbf{m} \times \mathbf{p}) \times \mathbf{m}, \quad (\text{A1})$$

where γ and α are the gyromagnetic ratio and the damping constant, respectively. The effective field \mathbf{H}_{eff} contains contributions from the external magnetic field, demagnetization field, exchange interaction, DMI, as well as the magnetic anisotropy. The thermal fluctuation field for a given temperature T is expressed as $\mathbf{H}_{\text{th}} = \mathbf{n}_{\text{ra}} \sqrt{2\alpha k_B T / (\mu_0 M_s \gamma \Delta V \Delta t)}$ [55], with k_B being the Boltzmann constant, μ_0 the vacuum permeability constant, and M_s the saturation magnetization. \mathbf{n}_{ra} is a unit vector with its orientation, to describe the fluctuation, adopted randomly in both time and space domains. ΔV stands for the volume of each unit cell in space, and Δt is the time interval. The strength of dampinglike spin torque can be expressed in general by $H_j = j \hbar \theta_{\text{SH}} / (2\mu_0 M_s e t_z)$, where j and θ_{SH} represent the density of the driving current and spin polarization efficiency (corresponding to the spin Hall angle of HM1 for an in-plane driving current), respectively. \hbar and e correspond to the reduced Planck constant and elementary charge, respectively. t_z is the thickness of the ferromagnetic working layer. The polarization vector \mathbf{p} relies on the direction of driving current. For an out-of-plane injection current for skyrmion creation, \mathbf{p} is set to be antiparallel to the magnetization in the working layer. For an in-plane current for skyrmion motion, we set $\mathbf{p} = -\hat{y}$.

Taking CoFeB as our ferromagnetic working layer, we use the exchange coefficient $A = 16$ pJ/m, the perpendicular magnetocrystalline anisotropy constant $K = 1.2$ MJ/m³, and saturation magnetization $M_s = 1200$ kA/m [56]. Unless specified otherwise, the Dzyaloshinskii-Moriya exchange coefficients are adopted as $D_1 = 2.2$ mJ/m² (induced by HM1) [57] and $D_2 = -0.5$ mJ/m² (HM2) [58], which are experimentally achievable. The size of the ferromagnetic film is $256 \times 128 \times 1.5$ nm³ discretized by $4 \times 4 \times 1.5$ nm³ unit cells, whose three lengths are all shorter than the exchange length $l_{\text{ex}} = \sqrt{2A / (\mu_0 M_s^2)} = 4.2$ nm and the DMI-associated characteristic length $l_{\text{DMI}} = 2A / D_1 = 14.5$ nm [59], as required for the numerical convergence. With these parameters, the diameter of the skyrmion in the absence of driving current is around 32 nm at zero temperature. For the initialization process, we apply a current intensity 600 MA/cm² with duration of 1 ns into the round-shape region under the fixed layer, whose diameter is 48 nm. By taking $\theta_{\text{SH}} = 0.4$, the skyrmion is formed after about 0.3 ns.

APPENDIX B: EVALUATION OF DMI-INDUCED ENERGY BARRIER

In order to evaluate the energy barrier introduced by the local modification of DMI, we apply a strong local magnetic field (10 T) at a single unit cell to pin the skyrmion at different positions in the nanotrack and calculate the enhancement of the skyrmion potential energy due to local DMI from

$$V_{\text{DMI}} = \int_{\text{Under HM2}} D_2 [m_z (\nabla \cdot \mathbf{m}) - (\mathbf{m} \cdot \nabla) m_z] dV. \quad (\text{B1})$$

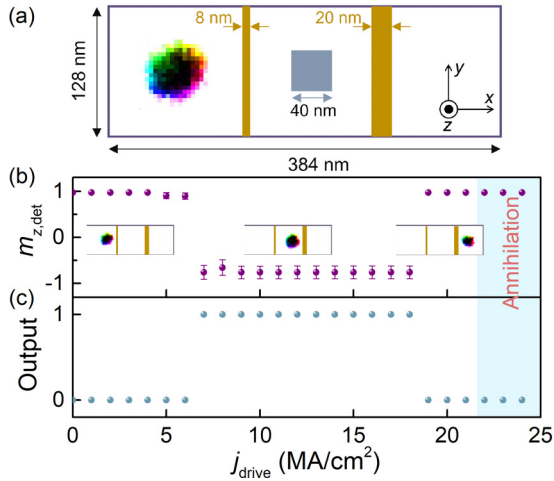


FIG. 6. (a) A sketch of the conservative logic device with two strips of heavy metals indicated by the yellow areas. The gray square represents the detection area. (b) Recorded magnetization $m_{z,\text{det}}$ of the ferromagnet at the detection area and (c) logic output as functions of the driving current j_{drive} . The insets in panel (b) show the snapshots of representative magnetization states. Here we take $T = 300$ K and $D_2 = -0.5$ mJ/m².

With the DMI-induced potential barrier and thermal fluctuation, the skyrmion center may slightly differ from the pinning site and can be described by the guiding center, $\mathbf{x}_s = \int \mathbf{x} \rho_{\text{id}} dV / \int \rho_{\text{id}} dV$ [60], averaging the topological density over the transient magnetic texture, i.e., $\rho_{\text{id}} = 1/(4\pi) \mathbf{m} \cdot (\partial_x \mathbf{m} \times \partial_y \mathbf{m})$ [61–63]. The results at zero temperature with different values of DMI modification and strip widths are plotted in Fig. 1(c).

According to Ref. [64], the DMI energy of the skyrmion fully outside the barrier area is given by $V_{\text{DMI}} = -2\pi^2 t_z D_1 R_s$, where R_s is the skyrmion radius determined by the real space contour with $m_z = 0$. As a rough estimation, we assume that this DMI energy is uniformly distributed within the skyrmion region of radius $2R_s$. The average DMI energy density in the skyrmion region then can be expressed as $-\pi t_z D_1 / (2R_s)$. When part of the skyrmion enters into the barrier region, in which the DMI density is enhanced by $\pi t_z |D_2| / (2R_s)$, it leads to an enhancement of the DMI energy. The maximal value is achieved when the skyrmion center arrives at the middle of the strip, where the overlap area between the strip and the skyrmion is around $4R_s w_2$ (assuming $w_2 \ll 2R_s$). The potential barrier thus can be expressed as Eq. (1), if one neglects the small distortion of the skyrmion texture introduced by the potential barrier. Taking $D_2 = -0.5$ mJ/m² and $w_2 = 8$ nm, we get $V_{\text{DMI}} \sim 3.8 \times 10^{-20}$ J, which shows a good agreement with the simulation result presented in Fig. 1(c).

APPENDIX C: CONSERVATIVE LOGIC DEVICE

As shown in Fig. 1(d), the output “0” contains a situation where the skyrmion is annihilated at the right edge. This asks for an initialization process to create another skyrmion for further logic operations. Alternatively, one may consider extending our model to a conservative device as sketched in Fig. 6(a), where a second wider strip defines the critical

current j_{c2} for skyrmion escaping from the detection region. The magnetization $m_{z,\text{det}}$ and logic readout of the working layer at the detection area are recorded as functions of the driving current in Figs. 6(b) and 6(c), with representative magnetization states displayed as insets. Accordingly, in the current range from 18 to 21 MA/cm², the skyrmion surviving in the nanotrack also gives the “0” output.

APPENDIX D: SKYRMION POTENTIAL ENERGY AT CRITICAL CURRENT J_{C1}

In the presence of a driving current, the driving force provides an additional contribution to the skyrmion potential energy with respect to the center of the strip (x_0) as

$$V_j(x_s) = \int_{x_s}^{x_0} \langle F_{\text{eff},x}(x) \rangle dx, \quad (\text{D1})$$

where the longitudinal component of the effective driving force derived from Eq. (A1) consists of the current-induced force and the dissipative one as [65]

$$\langle F_{\text{eff},x}(x) \rangle \approx \pi^2 \mu_0 H_j M_s t_z \langle R_s(x) \rangle - \frac{\alpha}{\gamma} \mu_0 M_s t_z \xi(x) \langle v(x) \rangle. \quad (\text{D2})$$

Here, $\langle \cdot \rangle$ stands for the average values from different calculations, eliminating the influence of thermal fluctuations

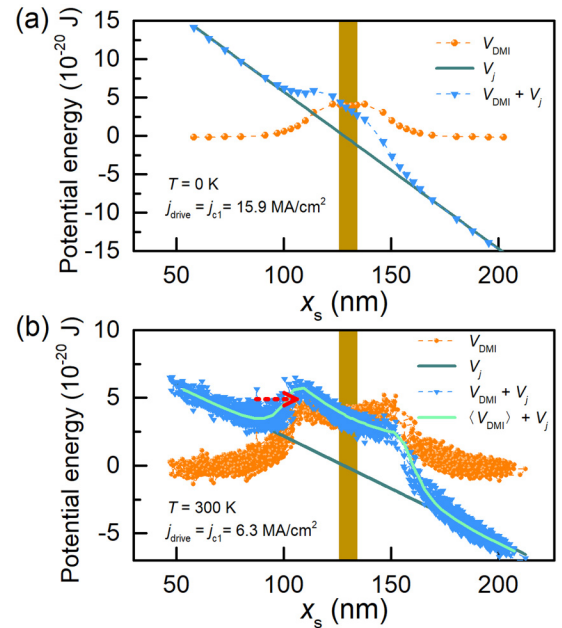


FIG. 7. Skyrmion potential energies due to local DMI (V_{DMI}) and driving current (V_j) with critical current $j_{\text{drive}} = 15.9$ MA/cm² at zero temperature and $j_{\text{drive}} = 6.3$ MA/cm² at 300 K. The average radius and skyrmion velocity extracted from micromagnetic simulation are 12.8 nm and 7.5 m/s for (a), and 24 nm and 9.8 m/s for (b), respectively. $\langle V_{\text{DMI}} \rangle$ in (b) corresponds to the effective DMI-induced potential energy calculated from an artificial zero-temperature skyrmion, whose radius is taken to be 24 nm, mimicking the simulated skyrmion at 300 K. The red dashed arrow indicates the path for skyrmion passing through the barrier associated by thermal fluctuation.

on the skyrmion radius (R_s) and its velocity (v). The dimensionless parameter ξ is approximately expressed as $\xi(x) \simeq 2\pi\sqrt{\langle R_s(x) \rangle^2 / l_{\text{DW}}^2 + 1} + 2\pi/\sqrt{\langle R_s(x) \rangle^2 / l_{\text{DW}}^2 + 1}$, with $l_{\text{DW}} = \sqrt{A/(K - \mu_0 M_s^2/2)}$ being the width of an effective static domain wall with the same material parameters [65]. The spatial dependence in $\langle R_s \rangle$ and $\langle v \rangle$ results from the interplay between the driving force and the barrier. For the sake of simplicity, at the critical current j_{c1} we further take their spatial averages, $\overline{\langle R_s \rangle}$ and $\overline{\langle v \rangle}$, along the skyrmion trajectory from its original location to x_0 . Equation (D1) thus reduces to

$$V_j(x_s) \simeq (x_0 - x_s) \overline{\langle F_{\text{eff},x} \rangle}. \quad (\text{D3})$$

At zero temperature, the thermal fluctuation is fully frozen out and the lower critical current with $\alpha = 0.5$ in Fig. 3(a) reads $j_{c1} = 15.9$ MA/cm², resulting in an average skyrmion radius $\overline{\langle R_s \rangle} \approx 12.8$ nm and a skyrmion velocity $\overline{\langle v \rangle} \approx 7.5$ m/s. The current-induced potential is plotted in Fig. 7(a), which nicely reflects the physics of the critical current, namely, with the driving force overcoming the DMI-

induced barrier and allowing the skyrmion passing through the barrier (see the total potential energy plotted as blue triangles). With the critical current $j_{c1} = 6.3$ MA/cm² at 300 K, we obtain $\overline{\langle R_s \rangle} \approx 24$ nm and $\overline{\langle v \rangle} \approx 9.8$ m/s and plot the current-induced potential as the olive curve in Fig. 7(b). Note that the average radius of the skyrmion at room temperature is about twice of that at zero temperature. To mimic its influence on the DMI-induced potential, we introduce a static zero-temperature skyrmion with its radius enlarged by a magnetic field of 8 mT in $-z$ direction and compute an effective value of $\langle V_{\text{DMI}} \rangle$. The total effective potential energy $\langle V_{\text{DMI}} \rangle + V_j$ is plotted as the cyan curve in Fig. 7(b), where a finite barrier remains. Alternatively, we calculate directly the DMI energy V_{DMI} at 300 K based on the pinning techniques explained in Appendix B and plot the numerical results of total potential energy $V_{\text{DMI}} + V_j$ collected from different simulations as blue symbols, which shows a strong fluctuation due to thermal effects. As one can see, although the average of the numerical $V_{\text{DMI}} + V_j$ seems to follow well with $\langle V_{\text{DMI}} \rangle + V_j$, the thermal fluctuation activates a path through the barrier as indicated by the red arrow.

-
- [1] B. Behin-Aein, D. Datta, S. Salahuddin, and S. Datta, Proposal for an all-spin logic device with built-in memory, *Nat. Nanotechnol.* **5**, 266 (2010).
- [2] N. Zhang, Y. Cao, Y. Li, A. W. Rushforth, Y. Ji, H. Zheng, and K. Wang, Complementary lateral-spin-orbit building blocks for programmable logic and in-memory computing, *Adv. Electron. Mater.* **6**, 2000296 (2020).
- [3] Z. Luo, A. Hrabec, T. P. Dao, G. Sala, S. Finizio, J. Feng, S. Mayr, J. Raabe, P. Gambardella, and L. J. Heyderman, Current-driven magnetic domain-wall logic, *Nature (London)* **579**, 214 (2020).
- [4] Y. Dong, T. Xu, H. Zhou, L. Cai, H. Wu, J. Tang, and W. Jiang, Electrically reconfigurable 3D spin-orbitronics, *Adv. Funct. Mater.* **31**, 2007485 (2021).
- [5] C. Wan, X. Zhang, Z. Yuan, C. Fang, W. Kong, Q. Zhang, H. Wu, U. Khan, and X. Han, Programmable spin logic based on spin Hall effect in a single device, *Adv. Electron. Mater.* **3**, 1600282 (2017).
- [6] G. J. Lim, D. Chua, W. Gan, C. Murapaka, and W. S. Lew, Programmable spin-orbit-torque logic device with integrated bipolar bias field for chirality control, *Adv. Electron. Mater.* **6**, 1901090 (2020).
- [7] X. Zhao, Y. Dong, W. Chen, X. Xie, L. Bai, Y. Chen, S. Kang, S. Yan, and Y. Tian, Purely electrical controllable complete spin logic in a single magnetic heterojunction, *Adv. Funct. Mater.* **31**, 2105359 (2021).
- [8] D. A. Allwood, G. Xiong, C. C. Faulkner, D. Atkinson, D. Petit, and R. P. Cowburn, Magnetic domain-wall logic, *Science* **309**, 1688 (2005).
- [9] S. Klingler, P. Pirro, T. Brächer, B. Leven, B. Hillebrands, and A. V. Chumak, Spin-wave logic devices based on isotropic forward volume magnetostatic waves, *Appl. Phys. Lett.* **106**, 212406 (2015).
- [10] W. Yu, J. Lan, and J. Xiao, Magnetic Logic Gate Based on Polarized Spin Waves, *Phys. Rev. Appl.* **13**, 024055 (2020).
- [11] A. V. Chumak, A. A. Serga, and B. Hillebrands, Magnon transistor for all-magnon data processing, *Nat. Commun.* **5**, 4700 (2014).
- [12] X. Zhang, M. Ezawa, and Y. Zhou, Magnetic skyrmion logic gates: Conversion, duplication and merging of skyrmions, *Sci. Rep.* **5**, 9400 (2015).
- [13] X. Xing, P. W. T. Pong, and Y. Zhou, Skyrmion domain wall collision and domain wall-gated skyrmion logic, *Phys. Rev. B* **94**, 054408 (2016).
- [14] H. Xia, C. Jin, C. Song, J. Wang, J. Wang, and Q. Liu, Control and manipulation of antiferromagnetic skyrmions in racetrack, *J. Phys. D: Appl. Phys.* **50**, 505005 (2017).
- [15] M. Fattouhi, K. Y. Mak, Y. Zhou, X. Zhang, X. Liu, and M. El Hafidi, Logic Gates Based on Synthetic Antiferromagnetic Bilayer Skyrmions, *Phys. Rev. Appl.* **16**, 014040 (2021).
- [16] S. Luo, M. Song, X. Li, Y. Zhang, J. Hong, X. Yang, X. Zou, N. Xu, and L. You, Reconfigurable Skyrmion logic gates, *Nano Lett.* **18**, 1180 (2018).
- [17] M. G. Mankalale, Z. Zhao, J.-P. Wang, and S. S. Sapatnekar, SkyLogic—A Proposal for a skyrmion-based logic device, *IEEE Trans. Electron Devices* **66**, 1990 (2019).
- [18] B. Paikaray, M. Kuchibhotla, A. Haldar, and C. Murapaka, Reconfigurable logic operations via gate controlled skyrmion motion in a nanomagnetic device, *ACS Appl. Electron. Mater.* **4**, 2290 (2022).
- [19] N. Sisodia, J. Pelloux-Prayer, L. D. Buda-Prejbeanu, L. Anghel, G. Gaudin, and O. Boulle, Programmable Skyrmion Logic Gates Based on Skyrmion Tunneling, *Phys. Rev. Appl.* **17**, 064035 (2022).
- [20] N. Sisodia, J. Pelloux-Prayer, L. D. Buda-Prejbeanu, L. Anghel, G. Gaudin, and O. Boulle, Robust and Programmable Logic-In-Memory Devices Exploiting Skyrmion Confinement and Channeling Using Local Energy Barriers, *Phys. Rev. Appl.* **18**, 014025 (2022).

- [21] M. Song, M. G. Park, S. Ko, S. K. Jang, M. Je, and K.-J. Kim, Logic device based on skyrmion annihilation, *IEEE Trans. Electron Devices* **68**, 1939 (2021).
- [22] Z. Yan, Y. Liu, Y. Guang, K. Yue, J. Feng, R. Lake, G. Yu, and X. Han, Skyrmion-Based Programmable Logic Device with Complete Boolean Logic Functions, *Phys. Rev. Appl.* **15**, 064004 (2021).
- [23] D. Yu, H. Yang, M. Chshiev, and A. Fert, Skyrmions-based logic gates in one single nanotrack completely reconstructed via chirality barrier, *Natl. Sci. Rev.* **9**, nwac021 (2022).
- [24] H. Zhang, D. Zhu, W. Kang, Y. Zhang, and W. Zhao, Stochastic Computing Implemented by Skyrmionic Logic Devices, *Phys. Rev. Appl.* **13**, 054049 (2020).
- [25] Y. Shu, Q. Li, J. Xia, P. Lai, Z. Hou, Y. Zhao, D. Zhang, Y. Zhou, X. Liu, and G. Zhao, Realization of the skyrmionic logic gates and diodes in the same racetrack with enhanced and modified edges, *Appl. Phys. Lett.* **121**, 042402 (2022).
- [26] X. Liang, J. Xia, X. Zhang, M. Ezawa, O. A. Tretiakov, X. Liu, L. Qiu, G. Zhao, and Y. Zhou, Antiferromagnetic skyrmion-based logic gates controlled by electric currents and fields, *Appl. Phys. Lett.* **119**, 062403 (2021).
- [27] U. K. Rößler, A. N. Bogdanov, and C. Pfleiderer, Spontaneous skyrmion ground states in magnetic metals, *Nature (London)* **442**, 797 (2006).
- [28] S. Mühlbauer, B. Binz, F. Jonietz, C. Pfleiderer, A. Rosch, A. Neubauer, R. Georgii, and P. Böni, Skyrmion lattice in a chiral magnet, *Science* **323**, 915 (2009).
- [29] B. Göbel, I. Mertig, and O. A. Tretiakov, Beyond skyrmions: Review and perspectives of alternative magnetic quasiparticles, *Phys. Rep.* **895**, 1 (2021).
- [30] N. Nagaosa and Y. Tokura, Topological properties and dynamics of magnetic skyrmions, *Nat. Nanotechnol.* **8**, 899 (2013).
- [31] G. Finocchio, F. Büttner, R. Tomasello, M. Carpentieri, and M. Kläui, Magnetic skyrmions: From fundamental to applications, *J. Phys. D: Appl. Phys.* **49**, 423001 (2016).
- [32] A. Fert, N. Reyren, and V. Cros, Magnetic skyrmions: Advances in physics and potential applications, *Nat. Rev. Mater.* **2**, 17031 (2017).
- [33] K. Everschor-Sitte, J. Masell, R. M. Reeve, and M. Kläui, Perspective: Magnetic skyrmions—Overview of recent progress in an active research field, *J. Appl. Phys.* **124**, 240901 (2018).
- [34] Y. Zhou, Magnetic skyrmions: Intriguing physics and new spintronic device concepts, *Natl. Sci. Rev.* **6**, 210 (2019).
- [35] X. Zhang, Y. Zhou, K. Mee Song, T.-E. Park, J. Xia, M. Ezawa, X. Liu, W. Zhao, G. Zhao, and S. Woo, Skyrmion-electronics: Writing, deleting, reading and processing magnetic skyrmions toward spintronic applications, *J. Phys.: Condens. Matter* **32**, 143001 (2020).
- [36] J. Sampaio, V. Cros, S. Rohart, A. Thiaville, and A. Fert, Nucleation, stability and current-induced motion of isolated magnetic skyrmions in nanostructures, *Nat. Nanotechnol.* **8**, 839 (2013).
- [37] K. Litzius, I. Lemesch, B. Krüger, P. Bassirian, L. Caretta, K. Richter, F. Büttner, K. Sato, O. A. Tretiakov, J. Förster, R. M. Reeve, M. Weigand, I. Bykova, H. Stoll, G. Schütz, G. S. D. Beach, and M. Kläui, Skyrmion Hall effect revealed by direct time-resolved x-ray microscopy, *Nat. Phys.* **13**, 170 (2017).
- [38] X. Ma, G. Yu, X. Li, T. Wang, D. Wu, K. S. Olsson, Z. Chu, K. An, J. Q. Xiao, K. L. Wang, and X. Li, Interfacial control of Dzyaloshinskii-Moriya interaction in heavy metal/ferromagnetic metal thin film heterostructures, *Phys. Rev. B* **94**, 180408(R) (2016).
- [39] S. Tacchi, R. Troncoso, M. Ahlberg, G. Gubbiotti, M. Madami, J. Akerman, and P. Landeros, Interfacial Dzyaloshinskii-Moriya Interaction in Pt/CoFeB Films: Effect of the Heavy-Metal Thickness, *Phys. Rev. Lett.* **118**, 147201 (2017).
- [40] R. Juge, K. Bairagi, K. G. Rana, J. Vogel, M. Sall, D. Maily, V. T. Pham, Q. Zhang, N. Sisodia, M. Foerster, L. Aballe, M. Belmeguenai, Y. Roussigné, S. Auffret, L. D. Buda-Prejbeanu, G. Gaudin, D. Ravelosona, and O. Boulle, Helium ions put magnetic skyrmions on the track, *Nano Lett.* **21**, 2989 (2021).
- [41] W. Zhang, H. Zhong, R. Zang, Y. Zhang, S. Yu, G. Han, G. L. Liu, S. S. Yan, S. Kang, and L. M. Mei, Electrical field enhanced interfacial Dzyaloshinskii-Moriya interaction in MgO/Fe/Pt system, *Appl. Phys. Lett.* **113**, 122406 (2018).
- [42] J. Torrejon, J. Kim, J. Sinha, S. Mitani, M. Hayashi, M. Yamanouchi, and H. Ohno, Interface control of the magnetic chirality in CoFeB/MgO heterostructures with heavy-metal underlayers, *Nat. Commun.* **5**, 4655 (2014).
- [43] J. Slonczewski, Current-driven excitation of magnetic multilayers, *J. Magn. Magn. Mater.* **159**, L1 (1996).
- [44] M. N. Baibich, J. M. Broto, A. Fert, F. N. Van Dau, F. Petroff, P. Etienne, G. Creuzet, A. Friederich, and J. Chazelas, Giant Magnetoresistance of (001)Fe/(001)Cr Magnetic Superlattices, *Phys. Rev. Lett.* **61**, 2472 (1988).
- [45] L. Shen, Y. Zhou, and K. Shen, Boundary-free spin torque nanoo oscillators based on ferrimagnetic skyrmions, *Appl. Phys. Lett.* **121**, 092403 (2022).
- [46] J. Iwasaki, M. Mochizuki, and N. Nagaosa, Current-induced skyrmion dynamics in constricted geometries, *Nat. Nanotechnol.* **8**, 742 (2013).
- [47] X. Zhang, G. P. Zhao, H. Fangohr, J. P. Liu, W. X. Xia, J. Xia, and F. J. Morvan, Skyrmion-skyrmion and skyrmion-edge repulsions in skyrmion-based racetrack memory, *Sci. Rep.* **5**, 7643 (2015).
- [48] P. Lai, G. P. Zhao, H. Tang, N. Ran, S. Q. Wu, J. Xia, X. Zhang, and Y. Zhou, An improved racetrack structure for transporting a skyrmion, *Sci. Rep.* **7**, 45330 (2017).
- [49] I. Purnama, W. L. Gan, D. W. Wong, and W. S. Lew, Guided current-induced skyrmion motion in 1D potential well, *Sci. Rep.* **5**, 10620 (2015).
- [50] W. Kang, Y. Huang, C. Zheng, W. Lv, N. Lei, Y. Zhang, X. Zhang, Y. Zhou, and W. Zhao, Voltage controlled magnetic skyrmion motion for racetrack memory, *Sci. Rep.* **6**, 23164 (2016).
- [51] D.-H. Jung, H.-S. Han, N. Kim, G. Kim, S. Jeong, S. Lee, M. Kang, M.-Y. Im, and K.-S. Lee, Magnetic skyrmion diode: Unidirectional skyrmion motion via symmetry breaking of potential energy barriers, *Phys. Rev. B* **104**, L060408 (2021).
- [52] A. Vansteenkiste, J. Leliaert, M. Dvornik, M. Helsen, F. Garcia-Sanchez, and B. Van Waeyenbergh, The design and verification of MuMax3, *AIP Adv.* **4**, 107133 (2014).
- [53] T. Gilbert, Classics in magnetism: A phenomenological theory of damping in ferromagnetic materials, *IEEE Trans. Magn.* **40**, 3443 (2004).
- [54] L. Shen, X. Li, J. Xia, L. Qiu, X. Zhang, O. A. Tretiakov, M. Ezawa, and Y. Zhou, Dynamics of ferromagnetic bimerons driven by spin currents and magnetic fields, *Phys. Rev. B* **102**, 104427 (2020).

- [55] X. Gong, K. Y. Jing, J. Lu, and X. R. Wang, Skyrmion pinning by disk-shaped defects, *Phys. Rev. B* **105**, 094437 (2022).
- [56] Z. Qin, Y. Wang, S. Zhu, C. Jin, J. Fu, Q. Liu, and J. Cao, Stabilization and reversal of skyrmion lattice in Ta/CoFeB/MgO multilayers, *ACS Appl. Mater. Interfaces* **10**, 36556 (2018).
- [57] M. Cubukcu, J. Sampaio, K. Bouzehouane, D. Apalkov, A. V. Khvalkovskiy, V. Cros, and N. Reyren, Dzyaloshinskii-Moriya anisotropy in nanomagnets with in-plane magnetization, *Phys. Rev. B* **93**, 020401(R) (2016).
- [58] Q. Y. Wong, W. L. Gan, F. L. Luo, G. J. Lim, C. C. I. Ang, F. N. Tan, W. C. Law, and W. S. Lew, In situ Kerr and harmonic measurement in determining current-induced effective fields in MgO/CoFeB/Ta, *J. Phys. D: Appl. Phys.* **51**, 115004 (2018).
- [59] Y. Li and H. Pang, Annihilation dynamics of magnetic skyrmion lattice state under in-plane magnetic field and spontaneous recovery after field removal, *Phys. Rev. B* **105**, 174425 (2022).
- [60] S. Komineas and N. Papanicolaou, Skyrmion dynamics in chiral ferromagnets, *Phys. Rev. B* **92**, 064412 (2015).
- [61] S.-Z. Lin, A. Saxena, and C. D. Batista, Skyrmion fractionalization and merons in chiral magnets with easy-plane anisotropy, *Phys. Rev. B* **91**, 224407 (2015).
- [62] J. Barker and O. A. Tretiakov, Static and Dynamical Properties of Antiferromagnetic Skyrmions in the Presence of Applied Current and Temperature, *Phys. Rev. Lett.* **116**, 147203 (2016).
- [63] J. Tang, Y. Wu, W. Wang, L. Kong, B. Lv, W. Wei, J. Zang, M. Tian, and H. Du, Magnetic skyrmion bundles and their current-driven dynamics, *Nat. Nanotechnol.* **16**, 1086 (2021).
- [64] X. S. Wang, H. Y. Yuan, and X. R. Wang, A theory on skyrmion size, *Commun. Phys.* **1**, 31 (2018).
- [65] L. Shen, J. Xia, G. Zhao, X. Zhang, M. Ezawa, O. A. Tretiakov, X. Liu, and Y. Zhou, Spin torque nano-oscillators based on antiferromagnetic skyrmions, *Appl. Phys. Lett.* **114**, 042402 (2019).